Modelling and simulation of CLC using a copper-based oxygen carrier in a double loop circulating fluidized bed reactor system

Yuanwei Zhang,*,† Øyvind Langørgen,‡ Inge Saanum,‡ Zhongxi Chao,¶ and Hugo A. Jakobsen†

†*Department of Chemical engineering, Norwegian University of Science and Technology, Sem Sælandsvei 4, 7034 Trondheim, Norway*

‡*SINTEF Energy Research, Sem Sælands vei 11, 7034 Trondheim, Norway*

¶*Safetec Nordic AS, Klæbuveien 194, 7037 Trondheim, Norway*

E-mail: yuanwei.zhang@ntnu.no

Abstract

In this work, a CFD simulator has been developed for a novel double loop circulating fluidized bed (DLCFB) reactor which is used for chemical looping combustion process. The simulator is implemented in an in-house code including the kinetic theory of granular flow and reaction models. Methane is used as fuel and copper oxide based particles used as oxygen carrier. The process is configured with an air reactor and a fuel reactor. The two reactors are modelled and solved by a sequential approach. The connection between the two reactors is realized through time-dependent inlet and outlet boundary conditions. The model is validated with the experimental data obtained in the current work. At a thermal input of 100 kW the methane conversion of 98 % was achieved. For the cases studied in this work, temperature is the most important factor

for the reactor performance, followed by the gas velocity and methane concentration of fuel. The increase of the methane concentration could decrease the methane conversion which is due to the decrease of specific inventory. As the gas velocity is increased, the residence time and the degree of gas-solid contact decreases, causing a decrease in reactor performance. Besides the effect of the single factor, the combination effect of the gas velocity and methane concentration is also important to the reactor performance.

1 Introduction

Global warming is arguably one of the greatest environmental challenges of the 21st century. It is recognized that the greenhouse gas emissions, especially the release of CO_2 from fossil fuel combustion, are likely to have been the dominant driver of such warming trend.[1] Chemical looping combustion (CLC) is an promising technology for CO_2 capture. It provides an efficient and low cost way for CO_2 capture because the separation of CO_2 is inherent to the process[2,3].

Typically, CLC system consists of two fluidized bed reactors, a fuel reactor (FR) and an air reactor (AR). A solid oxygen carrier (OC) is oxidized in the AR and reduced in the FR in a cyclical way. The principle of CLC is shown in Figure 1. In the fuel reactor, the fuel is oxidized by OC that is induced to $MeO_{\alpha-1}$ (equation 1). In the following step, this oxygen carrier is re-oxidized to the oxidation state with air in the AR (equation 2) and ready to start a new cycle. In this way, only CO_2 and H_2O are presented in the exhaust gas out of the FR, and after condensation of H_2O, pure CO_2 steam can be obtained for further processing. The sum of the two - step reactions (oxidation and reduction) of the CLC process is equivalent to the direct combustion of the fuel.

$$(2n+m)\mathrm{Me_xO_y} + \mathrm{C_nH_{2m}} \rightarrow (2n+m)\mathrm{Me_xO_{y-1}} + m\mathrm{H_2O} + \mathrm{nCO_2} \quad (1)$$

$$\mathrm{MeO_{y-1}} + \frac{1}{2}\mathrm{O_2} \rightarrow \mathrm{Me_xO_y} \quad (2)$$

A double loop circulating fluidized bed (DLCFB) reactor was proposed by SINTEF Energy Research and the Norwegian University of Science and Technology for the CLC process. The reactor concept is shown in Figure 2a. The objective for this design is to get sufficiently high fuel conversion, enhance the contact between fuel rich gaseous and OC. The reactor was designed for operation on methane as fuel gas with maximum thermal input of 150 kW[4]. Two circulating fluidized bed reactors are incorporated in the system and connected by cyclones, divided loop seals and a bottom extraction. The fuel gas and air are supplied to the bottom of each reactor. The solid entrained by one reactor will be led into the bottom of the other reactor. The FR is operated under the turbulent or fast fluidization regime in order to achieve better gas - solid contact despite the higher gas velocity will results the decrease of fuel residence time compared with the bubbling bed reactor. This special design also has the objective of flexible operation as for the oxygen carriers (OCs) and can be applied to other chemical looping process. The arrangement of the system is compact which is easy for scale up and operated under higher pressure as a further step.

Computational Fluid Dynamics (CFD) provides an efficient way to evaluate the performance of the reactive flow and improve the understanding of fluid dynamic and chemical process. The first CFD attempt for the CLC was performed by Jung and Gamwo,[5] followed by Deng et al.[6,7] and Jin et al.[8] Their work proved the capability of CFD method for modelling the reactive CLC process. But these studies were not validated by experiments. Mahalatkar et al.[9] verified capability of CFD method for exploring CLC by comparing the simulation results and experimental measurements. Up to data, the majority of the CLC simulation studies available in the literature were forced to the fuel reactor only[5–14]. Some authors have also carried out the full loop simulation. Kruggel-Emden et al.[11] simulated both reactors by using a dynamic inlet and outlet boundary coupled to the two reactors. 2D models with full CLC system (including cyclones and looping seals) were developed by Wang et al.,[15] Ahmed and Lu,[12] Su et al.[16] and Banerjee et al.[17] and the flow and reaction process were successfully predicted by their models. Besides the 2D models, the 3-D CLC simulations

combining hydrodynamics and reaction kinetics were performed by Parker[18] and Banerjee et al.[17] Much of the CFD work mentioned above are focused on studying the typical CLC setup with a bubbling bed reactor as FR and a riser reactor as AR. Little attempts[15,19,20] were carried out for other possible configurations.

A simulator has been developed for the CLC process in the DLCFB system in this study. The model is implemented by using FORTRAN language. Methane is used as the gaseous fuel and CuO is chosen as OC. The aim of the work including the model validation compared with the experimental data obtained within the project, and then since the concept of reactor design of DLCFB is still under development, another objective is to demonstrate the possibility of the reactor design for CLC process and provide detailed information which is difficult measured during the experiments. The fluidization regime, flow and reactive behaviour of gas and solid phase and the influence of operating conditions were investigated in this work.

2 Pilot unit

2.1 Overview of the CLC pilot unit

The DLCFB system consists of two interconnected circulating fluidized bed reactors as shown in Figure 2a. Two reactors (FR and AR) are interconnected through particle loop seals that work as gas locks to ensure that only the particles are transferred between the reactors. The solid flow out of one reactor could be transported to the other one or circulated back to the original reactor by utilizing the loop-seals. The AR riser has higher particle transport capacity compared to the FR riser because of higher flow area and higher gas volume flow. Therefore, a share of the particles need to go through the bottom extraction (lifter) back to the AR in order to bring as much particles back to AR as the AR brings to the FR. Up to a certain fuel power we can either operate the FR in CFB regime, feeding all particles upwards in the FR, or in the turbulent regime, feeding the particles through the lifter back

to the AR.

Both reactors are 6 m tall with an internal diameter of 0.23 m for the AR and 0.154 m for the FR. The reactors are heated up by hot air and fuel that are introduced into the particle beds, and pilot burners are mounted above the bed to ensure safe ignition of the injected fuel. During the CLC operation, the reactor temperature is controlled by adjusting the air preheat temperature to the air reactor. The system is designed for operation on methane as fuel gas at a maximum fuel power of 150 kW.

The system has two Teledyne 7500 IR gas analyzers measuring the CO, CO_2 and CH_4 concentration in the exhaust from of the two reactors. The oxygen concentration in the exhaust of the AR is collected by using Gasmet DX400 portable FTIR gas analyzer with an oxygen measuring cell. The local pressures are collected by pressure transducers which are installed along the reactor.

2.2 Test conditions

In the experiment, a Cu based OC was used because of its high reactivity, high transport capacity and low toxicity towards human beings[21]. The copper oxide impregnated on a commercially available γ -alumina support with a CuO content of 14.7 wt%. The particle density is 1700 kg/m^3 and the median diameter is 149 μm. The particle porosity is about 53 %.[22]

Before the experiment started the reactor system was filled with a certain amount of OC. Thereafter followed a heat-up sequence for about 5 hours using the air pre-heaters and the fuel gas lances in each reactor. When the reactor temperatures were above 1073 K, the pilot burners, the loop seals and lifter was shifted from air to CO_2 in order to achieve full CLC model. After the reactor system was in full CLC model, the fludization gas was shifted to nitrogen for the rest of the experiment.[23] The experimental results which used in the model validation section (5.2) are obtained by averaging 30 minutes when the system showed a stable performance after the fluidization gas was switched to nitrogen.

3 Computational model

3.1 Fluid dynamics model

A mathematical model for describing two - phase flow has been applied for investigating the behaviour of the gas and solid phase within the DLCFB reactor. An Eulerian approach is adopted with constitutive relations for the solid phase momentum transport based on the kinetic theory of granular flow (KTGF)..[24–27] The governing equations of the two phases are listed in Table 1. The standard $\kappa - \varepsilon$ turbulence model, listed in Tables S1 and S2, is used for describing the turbulence phenomena of the gas phase[27]. In the KTGF a granular temperature, Θ, is introduced for deriving the solid pressure and viscous stresses in order to closure the averaged model. Another important closure is the gas - solid drag force, which is the dominant force accounting the momentum exchange and driving the solids flow. In this study McKeen and Pugsley model[28] is used. All the closure equations are listed in Tables S3 and S4. The temperature is controlled within a narrow range by adjusting the air preheat temperature to the AR, thus the energy balance equations were not incorporated. The fluid dynamics model described above have already been validated in the previous publications.[29,30]

3.2 Reaction kinetics model

The OC is important for the CLC and several conditions are needed to be satisfied, such as highly reactive for the desired reactions, high oxygen transport capacity, mechanically stable over a large number of cycles under fluidization and relatively cheap. The OC used in the simulation is Cu-based particle as described in section 2. At the present temperature levels it is anticipated that the redox system will be CuO - Cu[31]. The reactions in the FR may include reaction (3)-(8). In this study, the reaction (3), (6) and (7) are simulated in the FR, as suggested by Abad et al.[32]. One step reaction is simulated in the AR, equation (9):

$$CuO + CH_4 \rightarrow CO + 2H_2 + Cu \tag{3}$$

$$3CuO + CH_4 \rightarrow CO + 2H_2O + 3Cu \tag{4}$$

$$CH_4 \rightarrow C + 2H_2 \tag{5}$$

$$C + H_2O \rightarrow CO + H_2 \tag{6}$$

$$CO + CuO \rightarrow CO_2 + Cu \tag{7}$$

$$H_2 + CuO \rightarrow H_2O + Cu \tag{8}$$

$$2Cu + O_2 \rightarrow 2CuO \tag{9}$$

The shrinking core model (SCM) was applied for the OC used in this study. Several studies[32–34] found that the reactions were controlled mainly by chemical reaction whilst gas film and ash layer resistance were negligible. In the simulation, the OC is characterized by uniform particles of constant diameter. The density of solid will be updated in accordance with the gas and solid mass transfer. The reaction model is:[32,34]

$$X = \frac{t}{\tau} \tag{10}$$

where X is the degree of conversion, τ is the time for complete conversion of the carrier and is calculated from:

$$\tau = \frac{r_g}{bV_M k C^n} \tag{11}$$

where C, n, ν, r_g and V_M represent the gas concentration, order of reaction, stoichiometric factor, mean radius of the grains, and molar volume, respectively. The reaction rate constant k is expressed by:

$$k = k_0 \exp(-E/RT) \tag{12}$$

where k_0 is the pre-exponential factor of the rate constant, also known as the frequency factor. E is the activation energy, R the ideal gas constant, ($R = 8.314\text{J/mol}^{-1}\text{K}^{-1}$).

The reaction rate of equation (3) - (6) is expressed as follows:

$$(-r)_i = \alpha_s \omega_{\text{CuO/Cu}} \left(\frac{\rho_M}{b} \frac{\mathrm{d}X}{\mathrm{d}t} \right)_i \tag{13}$$

where i, α_s, ω and ρ_M represent the ith reaction, solid volume fraction, CuO/Cu mass fraction and molar density. The detailed kinetic parameters are listed in table 2.[32,34]

The source term in the species mass balance equation for the j th species can be modelled by:

$$\Gamma_j^{\omega} = \nu_j M_j r \tag{14}$$

4 Interconnected reactor model and numerical considerations

4.1 Computational domain

The chemical looping combustion process is simulated by utilizing the DLCFB system as described in Section 2. The 2D plane geometry is chosen for the simulation of the fuel and air reactors, which is shown in Figure 2 (b), having the same dimensions as the experimental setup.

4.2 Numerical implementation of the coupling between the reactors

For the calculation, two different sets of coordinates and parameters are adopted to solve the governing equations for the AR and the FR respectively. The exchange of the solid flow

between the reactor units is realized through the time-dependent inlet and outlet boundary conditions, which is outlined below.

The total solid flow rate at the outlet of AR ($\dot{m}_{\mathrm{out,AR}}$) and FR ($\dot{m}_{\mathrm{out,FR}}$) are calculated as:

$$\dot{m}_{\mathrm{out,s,AR}} = \alpha_s \rho_s v_s A|_{\mathrm{out,AR}} \tag{15}$$

$$\dot{m}_{\mathrm{out,s,FR}} = \alpha_s \rho_s v_s A|_{\mathrm{out,FR}} \tag{16}$$

Since the AR riser has higher particle transport capacity compared to the FR riser, a share of the particles need to go through the lifter back to the AR in order to bring as much particles back to AR as the AR brings to the FR. The solid flow through the lifter is defined as $\dot{m}_{\mathrm{s,lifter}}$.

$$\dot{m}_{\mathrm{s,lifter}} = \dot{m}_{\mathrm{out,s,AR}} - \dot{m}_{\mathrm{out,s,FR}} \tag{17}$$

The inlet solid flow of the AR is the sum of the FR outlet solid flow $\dot{m}_{\mathrm{out,s,FR}}$, lifter flow $\dot{m}_{\mathrm{s,lifter}}$ and the change of gas flow rate across the AR $\triangle\dot{m}_{\mathrm{g,AR}}$.

$$\dot{m}_{\mathrm{in,s,AR}} = \dot{m}_{\mathrm{out,s,FR}} + \dot{m}_{\mathrm{s,lifter}} + \triangle\dot{m}_{\mathrm{g,AR}} \tag{18}$$

$$\dot{m}_{\mathrm{in,s,FR}} = \dot{m}_{\mathrm{out,s,AR}} - \dot{m}_{\mathrm{s,lifter}} + \triangle\dot{m}_{\mathrm{g,FR}} \tag{19}$$

The inlet solid condition (ω_{CuO}) of one reactor is set equal to the outlet solid condition of the other reactor:

$$\omega_{\mathrm{CuO}}|_{\mathrm{in,AR}} = \omega_{\mathrm{CuO}}|_{\mathrm{out,FR}} \tag{20}$$

$$\omega_{\mathrm{CuO}}|_{\mathrm{in,FR}} = \omega_{\mathrm{CuO}}|_{\mathrm{out,AR}} \tag{21}$$

The solution algorithm applied in this work is sketched in the Figure S1. With the input data and the estimation of coupling quantities, the FR is calculated first. In the FR calculation step, all variables inside the FR are obtained including the coupling quantities, for example the solid concentration, velocity and species mass fraction at the FR outlet. The AR calculation procedure is same as the FR except the inlet boundary conditions are determined in the FR step. After finishing the AR calculation, the results will update the FR boundary condition again. So the flow and reactive processes of the two reactors are simulated by a sequential approach. After a full loop is finished within the current time step, another computation loop for the next time step will run repeatedly.

4.3 Initial and boundary conditions

No fluidized gas is applied initially and the particles are in still state with $\alpha_s = 0.6$. The pressure drop across the gas distributor is assumed high enough, so the gas is supplied to the reactor inlets uniformly when $t > 0$. The solid flow feeding to one reactor is in line with the solid flow at the reactor outlet. For wall boundary condition, partial slip boundary condition[27] is used for solid phase and no-slip condition for gas phase. The normal velocities against the walls are equal to zero.

At the inlet, Dirchlet boundary condition[35] is used for scalar variables except pressure. For other boundaries, Neumann condition[35] is used. A fixed pressure is specified at the outlet and Neumann conditions are adopted for other boundary condition of pressure correction equation.

4.4 Numerical consideration

The model equations described in section 3 are discretized over a staggered grid arrangement with Finite Volume Method (FVM). The algorithm used in this study is inspired by the work by Lindborg,[36] Chao[37] and Jakobsen.[27] The second order central differential scheme is used for the diffusion term discretizing. A TVD scheme[38,39] is adopted for the convention term

discretizing, which gives higher order accuracy as well as the lower oscillation. For solving the coupled velocity and pressure, SIMPLE algorithm is widely used for the multiphase flow simulation. The pressure correction equation developed by Jakobsen[27] is used for solving the reactive two - phase flow. The discretized linear equations are solved by BCG algorithm.[36]

Since the reaction could be highly coupled with the species concentration and transport phenomena, special treatment is needed for solving the species mass balance especially for the fast reactions in which the species concentration can change dramatically. In this content, simultaneous, implicit treatment of transport- and reaction terms could be a natural choice. However such an approach would lead to very large systems of stiff, non-linear equations, whose solution would require excessive memory and computational costs. Thus, a fraction step method, which has been used successfully in solving the reactive two-phase flow, is used in this study. In this method, the species mass balance is integrated by additively splitting the equation into one flow part and one reaction part, respectively. These are sequentially integrated using the implicit Euler scheme. In the first step, the flow part is solved using the standard FVM:

$$\int_{\Delta V} \frac{{\alpha_k}^n {\rho_k}^n}{\Delta t}(\omega^*_{k,j} - \omega^n_{k,j})dv = -\int_{\Delta V} \nabla \cdot (\alpha^n_k \rho^n_k \vec{v}^n_k \omega^*_{k,j})dv - \int_{\Delta V} \nabla \cdot (\alpha^n_k \rho^n_k D^e_{k,j} \nabla \omega^*_{k,j})dv \quad (22)$$

Afterwards, in a second step, the chemical reactions are solved by:

$$\int_{\Delta V} \frac{{\alpha_k}^n {\rho_k}^n}{\Delta t}(\omega^{n+1}_{k,j} - \omega^*_{k,j})dv = \int_{\Delta V} (\Gamma^{\omega}_{k,j})^{n+1} dv \quad (23)$$

The resulting set of algebraic equations is then solved using a Broyden subroutine[40].

5 Results and discussion

The first part of this section presents the resolution study and the validation of the model. Then numerical experiments have been performed in order to explore the chemical process performance of CLC in the DLCFB reactor. The reactors geometric, solid property and operating conditions are shown in the Table 4. Simulation parameters are listed in Table 5. All simulations were run for 20 s and the results were averaged from 15 s to 20 s.

5.1 Resolution study

Choosing the optimum grid resolution is a non-trivial task for CFD studies. If larger grid sizes are used, the model may not capture the fluid dynamics and reaction kinetics occurring within the reactor accurately. Three different resolutions (0.015 m $\times$ 0.005 m, 0.0075 m$\times$ 0.005 m, 0.006 m$\times$ 0.005 m) were used for the calculation domain. For comparison, axial distribution of the solid hold-ups with the three grid resolutions are shown in Figure 3. It can be seen that the distribution of solid hold-up predicted by coarse gird is more homogeneous compared with other grid sizes. That is because when coarse grid was used, the different structures inside the fluidized beds are not properly resolved which results in the overestimation of the inter-phase momentum exchange.

In order to quantify the influence of grid resolution on chemical reactions, the axial distribution of methane (FR) and oxygen (AR) were also examined, as shown in Figure 4. The reactive performance on the AR side is not sensible with the grid size, which is due to the high reaction rate of oxidation and almost compete conversions were achieved in all cases. On the FR side, coarse grid under-estimated the reaction rate of reduction and the difference of results between the medium- and fine resolution is much lower. Considering the simulation time and the numerical accuracy, medium grid was chosen for the further simulations.

5.2 Validation of the coupled CFB model

In this section, the validation of the model was performed by comparing the simulation results and the experimental data within the project. The initial inventory for the simulation is estimated from the pressure drop obtained from the experiments.

Figure 5 depicts the pressure curve along with the height in the FR and AR respectively. Generally, the CFD calculation gives good agreement with the experimental data for both reactors. There are some discrepancies occurred in the lower part of the reactors. One possible reason for the deviation might due to the simplification of the inlet gas distribution of the simulation, which is not in line with the experiments. Another possible reason of the differences might due to the inventory used in the simulation is somewhat lower than the experiments. As mentioned above, the solid inventory in the simulation is estimated from the experimental pressure date along the whole reactor. However the first pressure transducer in the FR is placed 0.35 m above the gas distributor, which means the solid existed under the first pressure transducer is missing in the simulation. The missing particle could be approximated by the pressure drop between the first pressure tap above the gas distributor and the first one below the gas distributor. But this pressure drop also includes the pressure drop caused by the gas distributor, which is difficult to be estimated.

Axial distribution of different gas species and the corresponding dry gas compositions at the outlets of the two reactors are shown in Figure 6. It can be seen that the concentration of CH_4 and O_2 are decreased with the height of the reactors. The intermediate products, H_2 and CO, are maintained at low concentration since they disappear faster than they are generated. The outlet concentrations of different components show reasonable agreement with the measurements despite a over-prediction with the CH_4 and O_2 conversion. This can be explained as the CuO used in the current study is slight different from the literature,[32,34] which would lead to a certain amount of uncertainties of the kinetic parameters. The reactor performance can be characterised by CH_4 conversion, which expressed as:

$$X_{\mathrm{CH_4}} = 1 - \frac{\dot{n}_{\mathrm{CH_4,out}}}{\dot{n}_{\mathrm{CH_4,in}}} \tag{24}$$

in which $\dot{n}_{\mathrm{CH_4}}$ is the CH_4 molar flow at the inlet or outlet. The methane conversion in the experiment and simulation was above 98 % when the thermal input is 100 kW. At the same time, the specific fuel reactor inventory from the experiment was just about 100 kg/MW, which is lower compared to data found in the literature.

5.3 The characteristics of hydrodynamics and chemical process

Gas and solid flow behaviour of the fluidized bed reactor are highly related with the flow regime. In order to analysis the flow regime of the reactors under certain condition, the probabilistic averaging approach is used. The probabilities of the fluidized bed reactor operated under entrain flow regime can be calculated by imposing a probability density function (PDF), utilizing the transition velocities and the uncertainty associated with them. A normal distribution presented by[41] was used in the present work.

$$P_{bubb} = P(U^* > U_c^*) = 1 - [1 + \exp(-\frac{1.7(U^* - U_c^*)}{\sigma_c^*})]^{-1} \tag{25}$$

$$P_{fast} = P(U^* > U_{se}^*) = [1 + \exp(-\frac{1.7(U^* - U_{se}^*)}{\sigma_{se}^*})]^{-1} \tag{26}$$

$$P_{turb} = 1 - P_{fast} - P_{bubb} \tag{27}$$

The regime transition velocities and corresponding standard deviations are listed in table 3. As shown in Figure 7a, the FR is operated under the turbulent fluidization when the thermal input is 100 kW, but the possibilities are different along with the height. For example, there are some possibilities of being in bubbling bed at the lower part of the FR; whereas at the upper part of the reactor, the flow has the trend of being in the fast fluidization regime. This is because the additional gas production by CH_4 oxidation (one mole of CH_4

input gives three mole gas of CO_2 and H_2O output) which will increase the gas velocity of the FR, as shown in Figure 8b. When looking at the Figure 7b, it can be observed that the AR is more likely operated in the turbulent fluidization regime, similar with FR. But the possibility of being under the fast fluidization in the AR is much higher than the FR side, which is because the gas velocity in the AR is higher than the FR.

Figure 8a shows the solids concentration versus the height of the two reactors. Two regions, the bottom dense region and the dilute region, can be observed for both reactors. The transition zone in the AR is smoother compared with FR. The axial distribution of the gas velocity and the gas density are displayed in Figure 8b and Figure 8c, the gas density in the FR increase along the reactor due to the production of heavier gas (CO_2 and H_2O). On the contrary, the gas density and velocity in the AR decrease because the consumption of O_2.

Figure 9 illustrate the 2D distribution of CH_4, CO_2, H_2 in the FR and O_2 in the AR. The unconverted CH_4 is higher in the core region than near the walls, which is due to the core-annulus particle distribution. The reaction rate near the wall is enhanced, which results lower methane concentration. The opposite trend can be observed when looking at the CO_2 distributions. As intermediate products, H_2 concentration increases near the inlet and then decreases with the height of the FR. Regarding the O_2 distribution in the AR, more uniform radial distribution can be observed.

5.4 Effect of operation conditions

The simulations were designed and processed using the experimental design procedure known as factorial design.[42] Such a design allows for the statistical quantification of the significance of the effect that each independent variable has on each dependent variable and also describes the effect of two or more factors. Four factors, gas velocity of FR, temperature, methane concentration of fuel and air to fuel ratio, were selected for the simulations. Table 6 summarized the simulation matrix. The dependent variable of X_{CH_4}, indicating the performance of

CLC, was also included in Table 6.

The analysis of variance (ANOVA) is reported in Table 7. In the ANOVA, p-value is an indicator for determining the significance of a factor. It denotes the chance of observed result occurs by assuming the null hypothesis is true. Low p-value, normally smaller than 0.05, will reject the null hypothesis and the corresponding factor is believed to be statistically important. The main effect plot for CH_4 conversion and the normal plot of effects corresponding to the ANOVA are shown in Figures 10 and 11. The significant factors are those that deviated from the linear line. The results show that the temperature (B) has the largest influence on the reactor performance within the testing cases, followed by the gas velocity in the FR (A) and methane concentration (C). Temperature has the positive effect on the methane conversion, whereas the gas velocity in the FR and methane concentration of fuel have negative effect. Besides that, the effects of combination factor of AC are also significant for the reactor performance.

The positive effect caused by temperature can be explained by reaction model (equation 10 - 13). The higher temperature will increase the reaction rate and improve the reactor performance. Simulation above 1120 K was not performed since the observed attrition effect of the particles caused by high temperature[43] was not considered in the mathematics model.

A higher methane concentration produces an increase of the CH_4 molar flow when the gas velocity is maintained. That means the thermal input is increased (e.g. from 92 kW in case 6 to 147 kW in case 7), thereby the ratio between the fuel and the OC increased and the specific fuel reactor inventory is decreased. That is the main reason for the decrease of the CH_4 conversion. So it is clear that an increase in methane concentration has to be balanced by a decrease in fluidization velocity in order to keep the reactor performance.

For the effect of gas velocity, the reason for the negative effect on the reactor performance is because the higher gas velocity decrease the fuel residence time. Figure 12 also shows the regime possibility in FR is changed when the gas velocity increased. When the gas velocity increase from 2 m/s (case 11) to 3 m/s (case 12), the fluidization regime in upper part of FR

changed from turbulent regime to fast fluidization regime. When look at the OC conversion in Figure 14, higher velocity (case 12) results lower OC conversion. However, since the gas velocity increased, the solid circulating rate is also increased, that might have somehow positive effect for the reactor performance. On the AR side, since the air to fuel ratio is maintained, when the gas velocity of the FR increased, the gas velocity in the AR is also increased, that will driving the AR to the fast regime completely, as shown in Figure 13. Therefore as the gas velocity increases, the fuel residence time and the degree of gas-solid contact will decreases.

6 Conclusion

This study investigated the performance of CLC process in a novel DLCFB reactor by using a simulator which is developed by FORTRAN. Methane was chosen as fuel and porous copper oxide based particles was used as oxygen carrier. The model predicts reasonable results compared with the experimental data obtained within the project. The conclusions based on the simulation experiments are listed below:

- The reactive performance in the AR is not sensible with the grid size, which is due to the high reaction rate. Fine grid gives higher conversion on the FR side.
- At a thermal input of 100 kW, both reactors are operated in the turbulent regime and the methane conversion of 98 % was achieved. At the same time, the specific fuel reactor inventory was just about 100 kg/MW, which is lower compared to data found in the literature.
- Temperature has the largest influence on the reactor performance under the current conditions, followed by the gas velocity and methane concentration of fuel feeding to the FR. The effect of combination of gas velocity and methane concentration is also significant for the reactor performance.

- The increase of the methane concentration of fuel could decrease the specific inventory, which is the main reason for the negative effect of the pressure. The effect of gas velocity is due to the transition of flow regime and the resident time of the fuel.
- The turbulent fluidization regime gives a better CLC performance for the DLCFB reactor, which is due to the better contact between the OC and methane compared with the fast fluidization regime.

Supporting Information

The Supporting Information is available free of charge on the ACS Publications website. Gas turbulence model, the internal- and inter-phases constitutive equations and the solution algorithm.

Acknowledgement

This work is part of the BIGCLC project supported by the Research Council of Norway (224866) and the BIGCCS Centre, performed under the Norwegian research program Centres for Environment-friendly Energy Research (FME). The authors acknowledge the following partners for their contributions: Gassco, Shell, Statoil, TOTAL, ENGIE and the Research Council of Norway (193816/S60).

Nomenclature

Roman Symbols

Symbol	Description	Unit
A	cross-sectional area	m^2

b	stoichiometric factor	$-$
C	gas concentration	$\mathrm{mol/m^3}$
C_1, C_2, C_b, C_μ	turbulence model parameter	-
d_s	particle diameter	m
D_{ji}	binary diffusion coefficient	$\mathrm{m^2/s}$
$D_{k,j}$	diffusion coefficient for component j in phase k	$\mathrm{m^2/s}$
E	activation energy	kJ/mol
e	coefficient of restitution	-
g_0	radial distribution function	-
k	reaction rate coefficient	$\mathrm{mol^{1-n}m^{3n-2}/s}$
k_g	gas turbulent kinetic energy	$\mathrm{m^2/s^2}$
M	mole mass	kg/kmol
n	reaction order	$-$
P_j	probability of being in regime j	Pa
p_k	pressure of phase k	Pa
Pr	Prandtl number	-
R	gas constant	J/mol/K
r	reaction rate	$\mathrm{mol/m^3/s}$
r_g	radius of a grain	m
Re	Reynolds number	-

Re_p	particle Reynolds number	-
S_t	turbulent kinetic energy production	kg/ms^3
T	temperature	K
t	time	s
U^*	dimensionless superficial gas velocity	$-$
U_c^*	normalized transition velocity from bubbling to turbulent fluidization	$-$
U_{se}^*	normalized transition velocity to fast fluidization	$-$
V_M	molar volume	m^3/mol
X	conversion	-
Y_j	mass fraction of j	-
z	axial coordinate	m
$\bar{\bar{\mathrm{I}}}$	unit tensor	-
$\dot{m}$	mass flow rate	kg/s
$\vec{g}$	gravity acceleration	m/s^2
$\vec{M}_k$	interfacial momentum transfer of phase k	kg/m^2s^2
$\vec{v}_k$	velocity of phase k	m/s

Greek Symbols

Symbol	Description	Unit

α_k	volume fraction of phase k	-
$\bar{\bar{\tau}}_k$	stress tensor of phase k	N/m^2
$\bar{\bar{\tau}}_t$	turbulent stress tensor	N/m^2
β	inter-phase momentum transfer coefficient	kg/m^3s
Γ	interfacial mass transfer rate	kg/m^3m
γ_s	collisional energy dissipation	J/m^3s
κ_s	conductivity of granular temperature	kg/ms
λ_k	thermal conductivity of phase k	m^2/s
μ_k	viscosity of phase k	kg/ms
ν_j	stoichiometric coefficient	-
ω	mass fraction	-
ρ	density	kg/m^3
ρ_M	molar density	mol/m^3
τ	time for complete solid conversion	s
Θ	granular temperature	m^2/s^2
ε_g	turbulent energy dissipation rate	m^2/s^3

Subscripts

Symbol	Description	Unit

AR/FR	air reactor or fuel reactor	-
B	bulk	-
$bubb$	bubbling fluidization regime	-
$fast$	fast fluidization regime	-
i	reaction number	-
in	inlet	-
k	gas(g) or solid(s) phase	-
$lifter$	lifter	-
mf	minimum fluidization	-
out	outlet	-
t	turbulent	-
$turb$	turbulent fluidization regime	-

Superscripts

Symbol	Description	Unit
0	initial	-
$dilute$	dilute	-
e	effective	-
m	molecular	-
max	maximum	-

References

(1) IEA, *World Energy Outlook Special Report 2015: Energy and Climate Change*; OECD/IEA: Paris, 2015.

(2) Ishida, M.; Jin, H. A Novel Chemical-looping Combustor Without NOx Formation. *Ind. Eng. Chem. Res.* **1996**, *35*, 2469–2472.

(3) Intergovernmental Panel on Climate Change (IPCC), *IPCC Special Report on Carbon Dioxide Capture and Storage. Prepared by Working Group III of the Intergovernmental Panel on Climate Change; Metz, B., O. Davidson, H. C. de Coninck, M. Loos, and L. A. Meyer (eds.)*; Cambridge University Press: Cambridge, United Kingdom and New York, NY, USA, 442 pp., 2005.

(4) Bischi, A.; Langørgen, Ø.; Saanum, I.; Bakken, J.; Seljeskog, M.; Bysveen, M.; Morin, J.-X.; Bolland, O. Design Study of a 150kWth Double Loop Circulating Fluidized Bed Reactor System for Chemical Looping Combustion with Focus on Industrial Applicability and Pressurization. *International Journal of Greenhouse Gas Control* **2011**, *5*, 467–474.

(5) Jung, J.; Gamwo, I. K. Multiphase CFD-based Models for Chemical Looping Combustion Process: Fuel Reactor Modeling. *Powder Technol.* **2008**, *183*, 401–409.

(6) Deng, Z.; Xiao, R.; Jin, B.; Song, Q.; Huang, H. Multiphase CFD Modeling for a Chemical Looping Combustion Process (Fuel Reactor). *Chem. Eng. Technol.* **2008**, *31*, 1754–1766.

(7) Deng, Z.; Xiao, R.; Jin, B.; Song, Q. Numerical Simulation of Chemical Looping Combustion Process with $CaSO_4$ Oxygen Carrier. *Int. J. Greenh. Gas Control.* **2009**, *3*, 368–375.

(8) Jin, B.; Xiao, R.; Deng, Z.; Song, Q. Computational Fluid Dynamics Modeling of Chemical Looping Combustion Process with Calcium Sulphate Oxygen Carrier. *Int. J. Chem. Reactor Eng.* **2009**, *7*, A19.

(9) Mahalatkar, K.; Kuhlman, J.; Huckaby, E. D.; O'Brien, T. Computational Fluid Dynamic Simulations of Chemical Looping Fuel Reactors Utilizing Gaseous Fuels. *Chem. Eng. Sci.* **2011**, *66*, 469–479.

(10) Kruggel-Emden, H.; Stepanek, F.; Munjiza, A. A Study on the Role of Reaction Modeling in Multi-phase CFD-based Simulations of Chemical Looping Combustion. *Oil Gas Sci. Technol.* **2011**, *66*, 313–331.

(11) Kruggel-Emden, H.; Rickelt, S.; Stepanek, F.; Munjiza, A. Development and Testing of an Interconnected Multiphase CFD-model for Chemical Looping Combustion. *Chem. Eng. Sci.* **2010**, *65*, 4732–4745.

(12) Bougamra, A.; Huilin, L. Modeling of Chemical Looping Combustion of Methane Using a Ni-based Oxygen Carrier. *Energy Fuels.* **2014**, *28*, 3420–3429.

(13) Guan, Y.; Chang, J.; Zhang, K.; Wang, B.; Sun, Q. Three-dimensional CFD Simulation of Hydrodynamics in an Interconnected Fluidized Bed for Chemical Looping Combustion. *Powder Technol.* **2014**, *268*, 316–328.

(14) Geng, C.; Zhong, W.; Shao, Y.; Chen, D.; Jin, B. Computational Study of Solid Circulation in Chemical-looping Combustion Reactor Model. *Powder Technol.* **2015**, *276*, 144–155.

(15) Wang, S.; Lu, H.; Zhao, F.; Liu, G. CFD Studies of Dual Circulating Fluidized Bed Reactors for Chemical Looping Combustion Processes. *Chem. Eng. J.* **2014**, *236*, 121–130.

(16) Su, M.; Zhao, H.; Ma, J. Computational Fluid Dynamics Simulation for Chemical Looping Combustion of Coal in a Dual Circulation Fluidized Bed. *Energy Convers. Manage.* **2015**, *105*, 1–12.

(17) Banerjee, S.; Agarwal, R. K. An Eulerian Approach to Computational Fluid Dynamics Simulation of a Chemical-Looping Combustion Reactor with Chemical Reactions. *J. Energy Res. Technol.* **2016**, *138*, 042201.

(18) Parker, J. M. CFD Model for the Simulation of Chemical Looping Combustion. *Powder Technol.* **2014**, *265*, 47–53.

(19) Hamilton, M. A.; Whitty, K. J.; Lighty, J. S. Numerical Simulation Comparison of Two Reactor Configurations for Chemical Looping Combustion and Chemical Looping with Oxygen Uncoupling. *J. Energy Resour. Technol.* **2016**, *138*, 042213, 1–9.

(20) Pröll, T.; Kolbitsch, P.; Bolhàr-Nordenkampf, J.; Hofbauer, H. A Novel Dual Circulating Fluidized Bed System for Chemical Looping Processes. *AlChE J.* **2009**, *55*, 3255–3266.

(21) Adanez-Rubio, I.; Arjmand, M.; Leion, H.; Gayan, P.; Abad, A.; Mattisson, T.; Lyngfelt, A. Investigation of Combined Supports for Cu-based Oxygen Carriers for Chemical-looping with Oxygen Uncoupling (CLOU). *Energy Fuels.* **2013**, *27*, 3918–3927.

(22) Cabello, A.; Gayán, P.; Abad, A.; de Diego, L.; García-Labiano, F.; Izquierdo, M.; Scullard, A.; Williams, G.; Adánez, J. Long-lasting Cu-based Oxygen Carrier Material for Industrial Scale in Chemical Looping Combustion. *Int. J. Greenhouse Gas Control.* **2016**, *52*, 120–129.

(23) Langørgen, Ø.; Saanum, I.; Haugen, N. E. L. Chemical Looping Combustion of Methane Using a Copper-based Oxygen Carrier in a 150 kW Reactor System. *Energy Procedia.* **2017**, *114*, 352–360.

(24) Jenkins, J.; Savage, S. A Theory for the Rapid Flow of Identical, Smooth, nearly Elastic, Spherical Particles. *J. Fluid Mech.* **1983**, *130*, 187–202.

(25) Lun, C.; Savage, S. B.; Jeffrey, D.; Chepurniy, N. Kinetic Theories for Granular Flow: Inelastic Particles in Couette Flow and Slightly Inelastic Particles in a General Flow field. *J. Fluid Mech.* **1984**, *140*, 223–256.

(26) Gidaspow, D. *Multiphase Flow and Fluidization: Continuum and Kinetic Theory Descriptions*; Academic press: San Diego, US, 1994.

(27) Jakobsen, H. A. *Chemical Reactor Modeling, Multiphase Reactive Flows,*, 2nd ed.; Springer-Verlag: Berlin, Germany: Springer-Verlag, 2014.

(28) McKeen, T.; Pugsley, T. Simulation and Experimental Validation of a Freely Bubbling Bed of FCC Catalyst. *Powder Technol.* **2003**, *129*, 139–152.

(29) Zhang, Y.; Chao, Z.; Jakobsen, H. A. Modelling and Simulation of Hydrodynamics in Double Loop Circulating Fluidizedbed Reactor for Chemical Looping Combustion Process. *Powder Technol.* **2017**, *310*, 35–45.

(30) Zhang, Y.; Chao, Z.; Jakobsen, H. A. Modelling and Simulation of Chemical Looping Combustion Process in a Double Loop Circulating Fluidized Bed Reactor. *Chem. Eng. J.* **2017**, *320*, 271–282.

(31) Penthor, S.; Zerobin, F.; Mayer, K.; Pröll, T.; Hofbauer, H. Investigation of the Performance of a Copper Based Oxygen Carrier for Chemical Looping Combustion in a 120kW Pilot Plant for Gaseous Fuels. *Appl. Energy.* **2015**, *145*, 52–59.

(32) Abad, A.; Adánez, J.; García-Labiano, F.; Luis, F.; Gayán, P. Modeling of the Chemical-looping Combustion of Methane Using a Cu-based Oxygen-Carrier. *Combust. Flame.* **2010**, *157*, 602–615.

(33) García-Labiano, J. A. A. A., L.F.de DIEGO; Gayán, P. Reduction and Oxidation Kinetics of a Copper-based Oxygen Carrier Prepared by Impregnation for Chemical-looping Combustion. *Ind. Eng. Chem. Res.* **2004**, *43*, 8168–8177.

(34) Abad, A.; Adánez, J.; García-Labiano, F.; Luis, F.; Gayán, P.; Celaya, J. Mapping of the Range of Operational Conditions for Cu-, Fe-, and Ni-based Oxygen Carriers in Chemical-looping Combustion. *Chem. Eng. Sci.* **2007**, *62*, 533–549.

(35) Weisstein, E. W. Boundary Conditions, From MathWorld–A Wolfram Web Resource. `http://mathworld.wolfram.comBoundaryConditions.html`.

(36) Lindborg, H. Modeling and Simulation of Reactive Two-Phase Flows in Fluidized Bed Reactors. Ph.D. thesis, Norwegian Institute of Technology, Trondheim, Norway, 2008.

(37) Zhongxi, C. Modeling and Simulation of Reactive Three-Phase Flows in Fluidized Bed Reactors: Application to the SE-SMR Process. Ph.D. thesis, Norwegian Institute of Technology, Trondheim, Norway, 2012.

(38) Van Leer, B. Towards the Ultimate Conservation Difference Scheme. II. Monotonicity and Conservation Combined in a Second-order Scheme. *J. Comput. Phys.* **1974**, *14*, 361–370.

(39) Van Leer, B. Towards the Ultimate Conservative Difference Scheme. IV. A New Approach to Numerical Convection. *J. Comput. Phys.* **1977**, *23*, 276–299.

(40) Press, W. H.; Teukolsky, S. A.; Vetterling, W. T.; Flannery, B. P. *Numerical Recipes in FORTRAN 77. The Art of Scientific Computing, volume 1*, 2nd ed.; Cambridge Univ. Press: New York, 1992.

(41) Abba, I. A.; Grace, J. R.; Bi, H.; Thompson, M. Spanning the Flow Regimes: Generic Fluidized-bed Reactor Model. *AIChE J.* **2003**, *47*, 1838–1848.

(42) Montgomery, D. C. *Design and Analysis of Experiments*, 5th ed.; John Wiley & Sons: New York, 2001.

(43) Forero, C.; Gayán, P.; García-Labiano, F.; De Diego, L.; Abad, A.; Adánez, J. High Temperature Behaviour of a CuO/γAl_2O_3 Oxygen Carrier for Chemical-looping Combustion. *Int. J. Greenhouse Gas Control.* **2011**, *5*, 659–667.

Table 1: Governing equations

Continuity equation for phase k $(k = g, s)$
$\frac{\partial}{\partial t}(\alpha_k \rho_k) + \nabla \cdot (\alpha_k \rho_k \vec{v}_k) = \Gamma_k$
Momentum equation for phase k $(k = g, s)$
$\frac{\partial}{\partial t}(\alpha_k \rho_k \vec{v}_k) + \nabla \cdot (\alpha_k \rho_k \vec{v}_k \vec{v}_k) = -\alpha_k \nabla p - \nabla \cdot \alpha_k \bar{\bar{\tau}}_k + \vec{M}_k + \alpha_k \rho_k \vec{g} + \Gamma_k^{\vec{v}}$
Species mass balance for phase k $(k = g, s)$
$\frac{\partial}{\partial t}(\alpha_k \rho_k \omega_{k,j}) + \nabla \cdot (\alpha_k \rho_k \vec{v}_k \omega_{k,j}) = \nabla \cdot (\alpha_k \rho_k D_{k,j}^e \nabla \omega_{k,j}) + \Gamma_{k,j}^{\omega}$
Gas turbulent kinetic energy equation
$\frac{\partial}{\partial t}(\alpha_g \rho_g k_g) + \nabla \cdot (\alpha_g \rho_g k_g \vec{v}_g) = \alpha_g(-\bar{\bar{\tau}}_t : \nabla \vec{v}_g + S_t) + \nabla \cdot (\alpha_g \frac{\mu_g^t}{\sigma_g} \nabla k_g) - \alpha_g \rho_g \varepsilon_g$
Gas turbulent energy dissipation rate equation
$\frac{\partial}{\partial t}(\alpha_g \rho_g \varepsilon_g) + \nabla \cdot (\alpha_g \rho_g \varepsilon_g \vec{v}_g) = \alpha_g C_1 \frac{\varepsilon_g}{k_g}(-\bar{\bar{\tau}}_t : \nabla \vec{v}_g + S_t) + \nabla \cdot (\alpha_g \frac{\mu_g^t}{\sigma_\varepsilon} \nabla \varepsilon_g) - \alpha_g \rho_g C_2 \frac{\varepsilon_g^2}{k_g}$
Granular temperature equation
$\frac{3}{2}\left[\frac{\partial}{\partial t}(\alpha_s \rho_s \Theta_s) + \nabla \cdot (\alpha_s \rho_s \Theta_i \vec{v}_s)\right] = -\bar{\bar{\tau}}_s : \nabla \vec{v}_s + \nabla \cdot (\kappa_s \nabla \Theta_s) - 3\beta\Theta_s - \gamma_s$

Table 2: Kinetic parameters[32,34]

	CH_4	H_2	CO	O_2
b	4	1	1	2
r_g	1.4×10^{-6}	1.4×10^{-6}	1.4×10^{-6}	2.3×10^{-10}
$k_0(\mathrm{mol^{1-n} m^{3n-2} s^{-1}})$	480	1.54×10^{-3}	2.21×10^{-4}	4.7×10^{-6}
E(kJ/mol)	106	20	11	15
n	0.5	0.5	0.8	1

Table 3: Summary of correlations for regime transition velocities[41]

Regime boundary correlation	Normalized standard deviation
$Re_c = 0.74 Ar^{0.426}$	$\sigma_c^* = 0.29$
$Re_{se} = 1.68 Ar^{0.469}$	$\sigma_c^* = 0.45$

Table 4: Main geometric and operating parameters

Description	Unit	Value
Reactor geometry		
AR height	m	6
AR diameter	m	0.23
FR height	m	6
FR diameter	m	0.154
Particle properties		
Mean particle size	μm	149
Particle density	kg/m^3	1700
Active CuO content	%	14.7
Operational condition		
Operating pressure	atm	1.0, 2.0
Lower heating value of fuel	MJ/kg	50
Inlet composition of FR	–	25 % CH_4, 75 % N_2
	–	40 % CH_4, 60 % N_2
Temperature in FR	K	1000, 1100
Temperature in AR	K	1000, 1100
Global air-fuel ratio	–	1.1, 1.4

Table 5: Important model inputs

Description	Unit	Value
Grid size	m	0.01× 0.005
Gas viscosity	kg/ms	1.82×10^{-5}
Sphericity of particle	–	1
Restitution coefficient of particles	–	0.99
Initial bed height of FR	m	0.65
Initial bed height of AR	m	0.75
Time step	s	1.0×10^{-4}

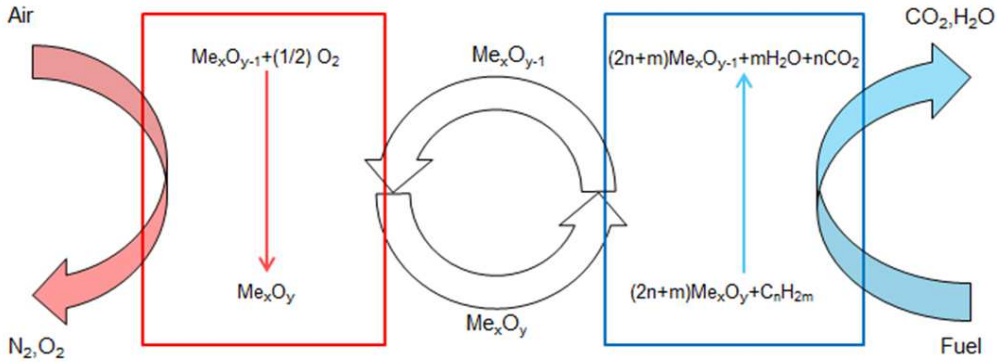

Figure 1: Schematic process diagram of CLC.

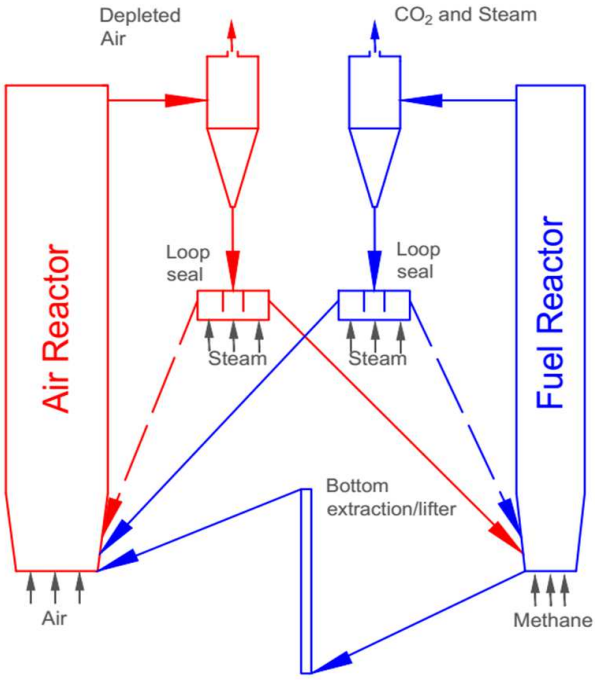

(a)

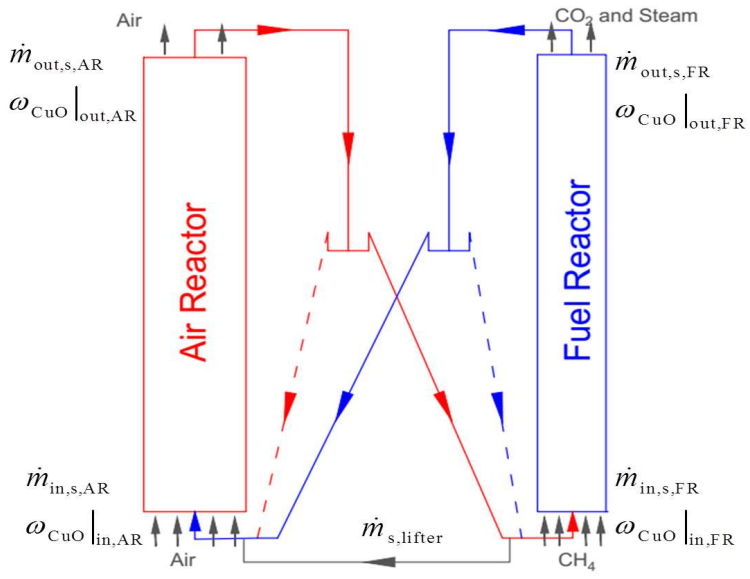

(b)

Figure 2: (a) Sketch of the double loop circulating fluidized bed reactor. (b) Schematic of the 2D computational domain

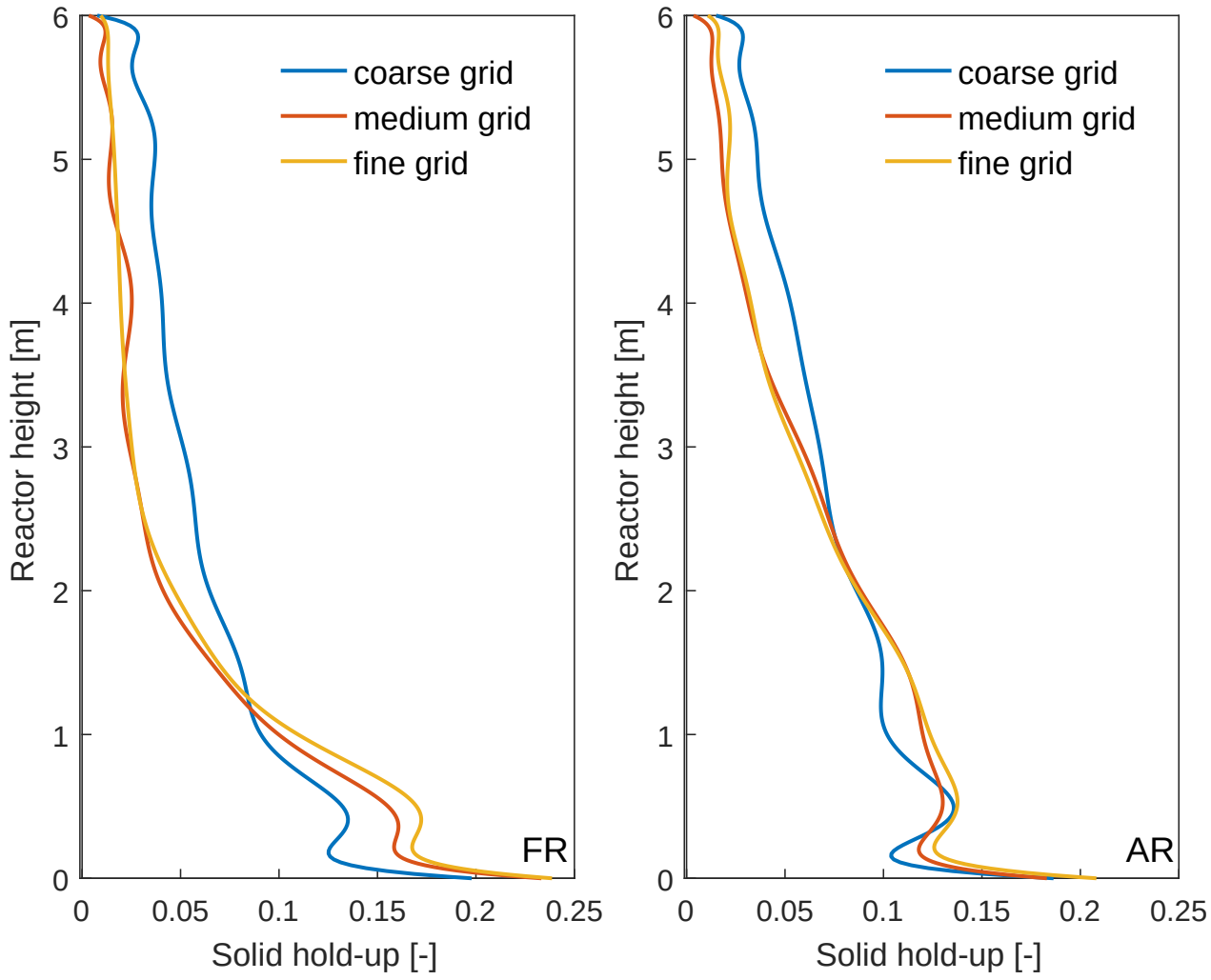

(a) (b)

Figure 3: Influence of grid resolution on numerical results (a) FR solid hold-up. (b) AR solid hold-up

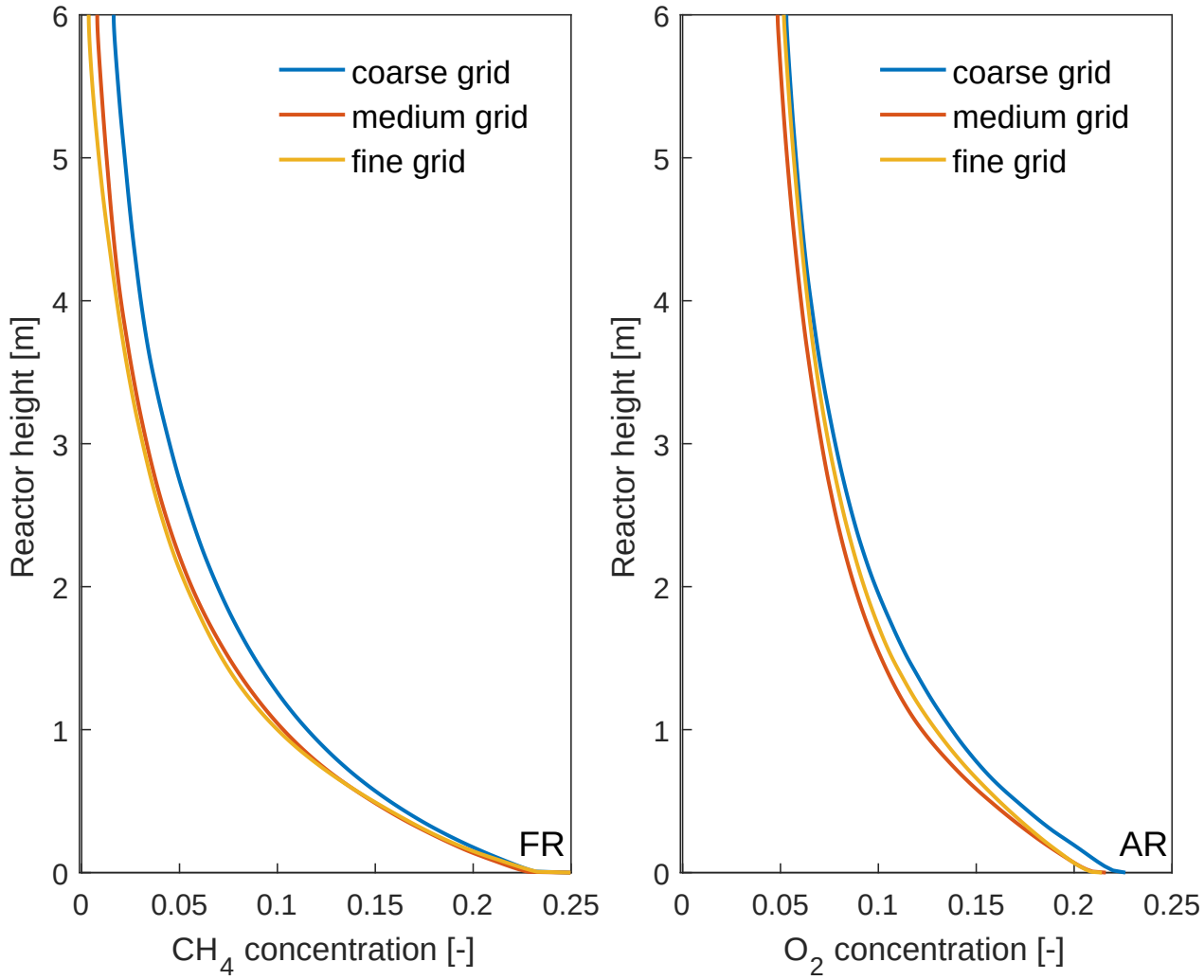

Figure 4: Influence of grid resolution on numerical results (a) Methane axial distribution. (b) Oxygen axial distribution

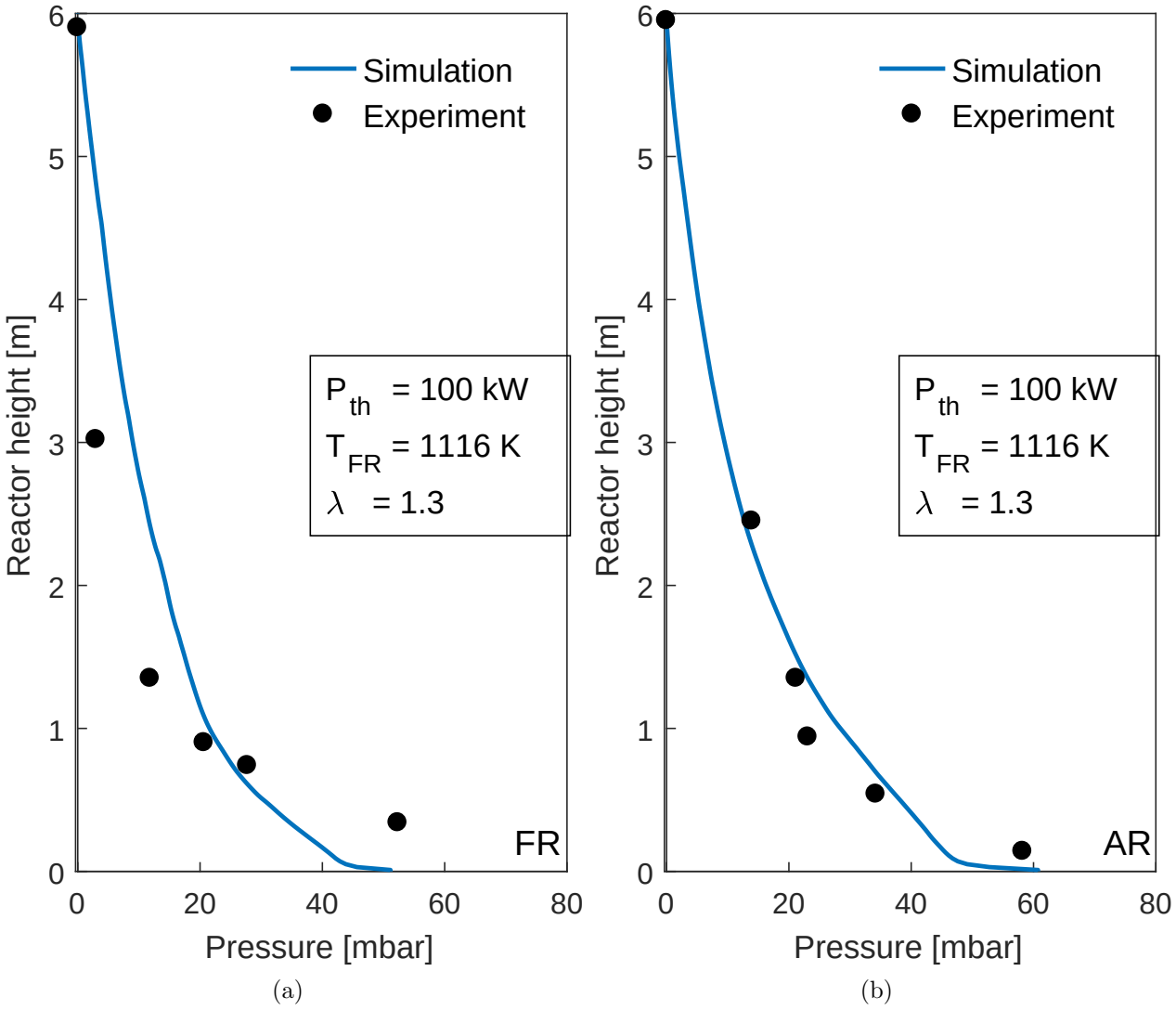

(a) (b)

Figure 5: Comparison of pressure profiles between simulation and experimental results.

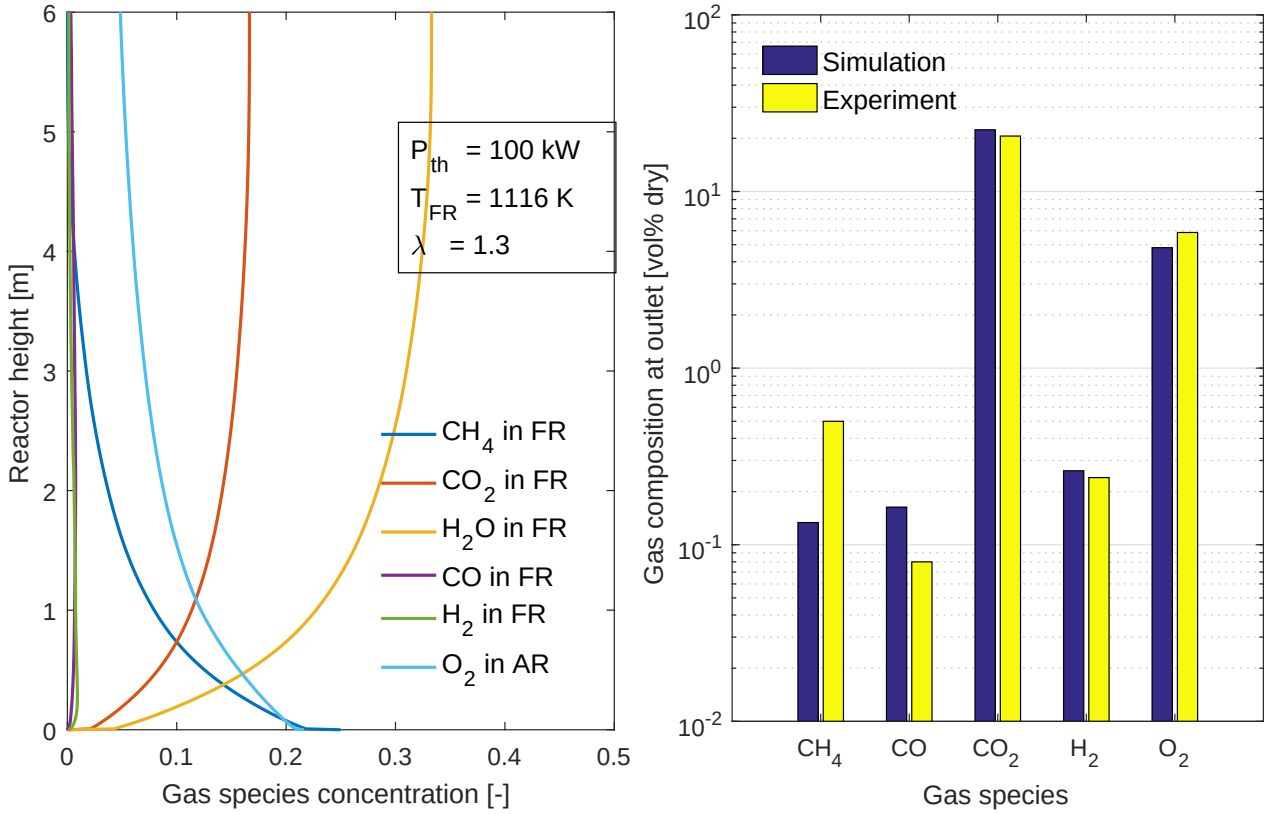

(a) (b)

Figure 6: Chemical reaction validation.

Table 6: Simulation matrix

Case	Gas velocity (m/s) (A)	Temperature (K) (B)	CH4 concentration (C)	Air to fuel ratio (D)	X_{CH_4}
1	2.0	1000	0.25	1.1	0.77
2	3.0	1000	0.25	1.1	0.46
3	2.0	1100	0.25	1.1	0.99
4	3.0	1100	0.25	1.1	0.72
5	2.0	1000	0.40	1.1	0.56
6	3.0	1000	0.40	1.1	0.41
7	2.0	1100	0.40	1.1	0.87
8	3.0	1100	0.40	1.1	0.70
9	2.0	1000	0.25	1.4	0.77
10	3.0	1000	0.25	1.4	0.49
11	2.0	1100	0.25	1.4	0.99
12	3.0	1100	0.25	1.4	0.81
13	2.0	1000	0.40	1.4	0.57
14	3.0	1000	0.40	1.4	0.42
15	2.0	1100	0.40	1.4	0.90
16	3.0	1100	0.40	1.4	0.74

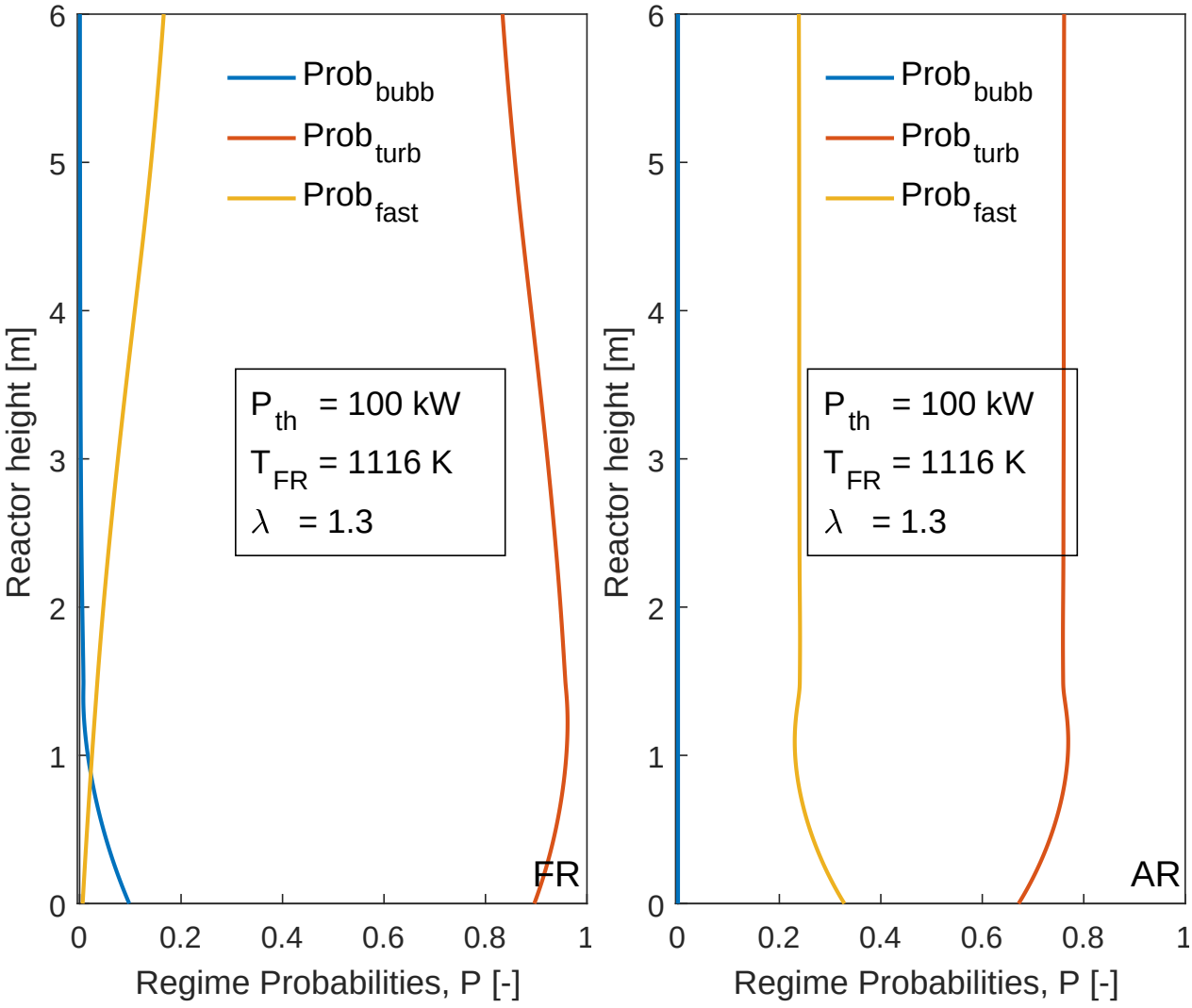

(a) (b)

Figure 7: Regime probability (a) FR. (b) AR.

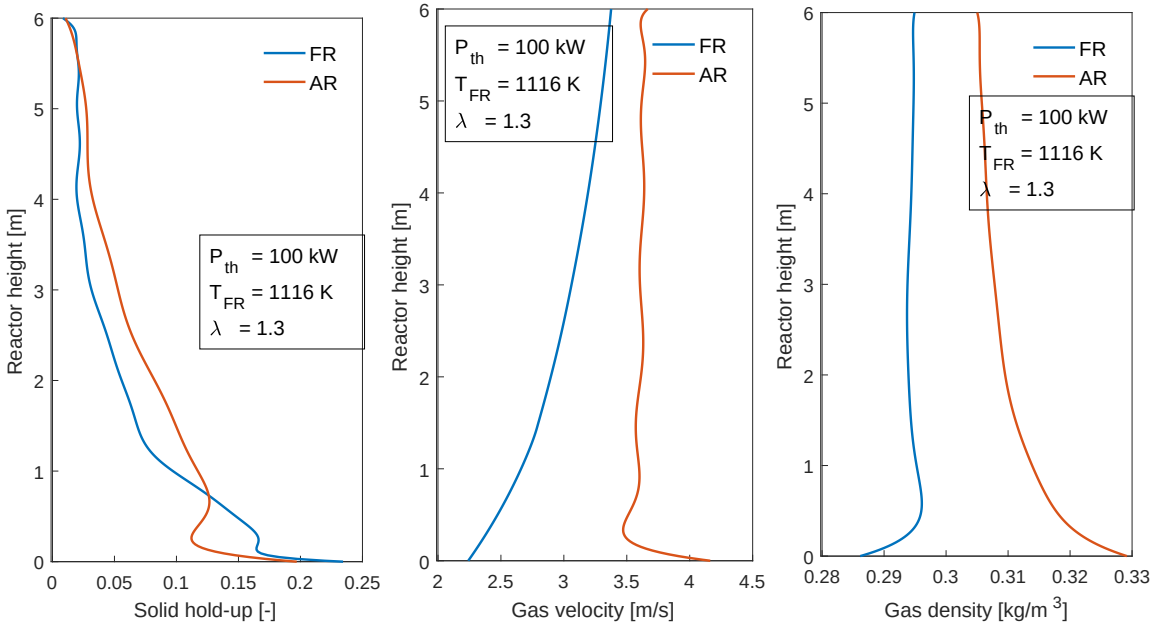

(a) (b) (c)

Figure 8: Axial distribution. (a) solid hold-up. (b) gas velocity. (c) gas density.

Table 7: ANOVA analysis

Effect	Degree of freedom	Sum of squares (%)	p-value
A	1	16.99	0.000
B	1	33.18	0.000
C	1	4.37	0.000
D	1	0.22	0.082
AB	1	0.03	0.434
AC	1	0.92	0.007
AD	1	0.12	0.168
BC	1	0.03	0.057
BD	1	0.08	0.226
CD	1	0.00	0.869
Error	5		
Total	15		

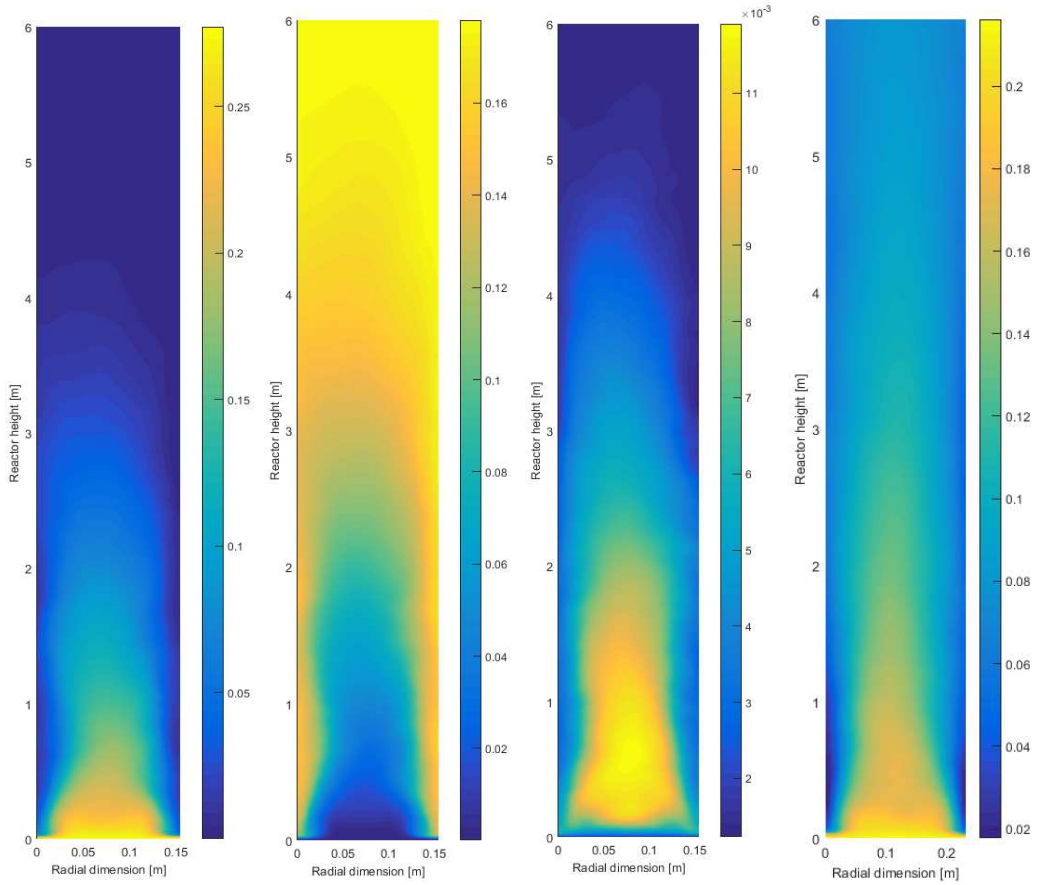

(a) (b) (c) (d)

Figure 9: 2D distribution of gas component (a) CH_4. (b) CO_2. (c) H_2. (d) O_2.

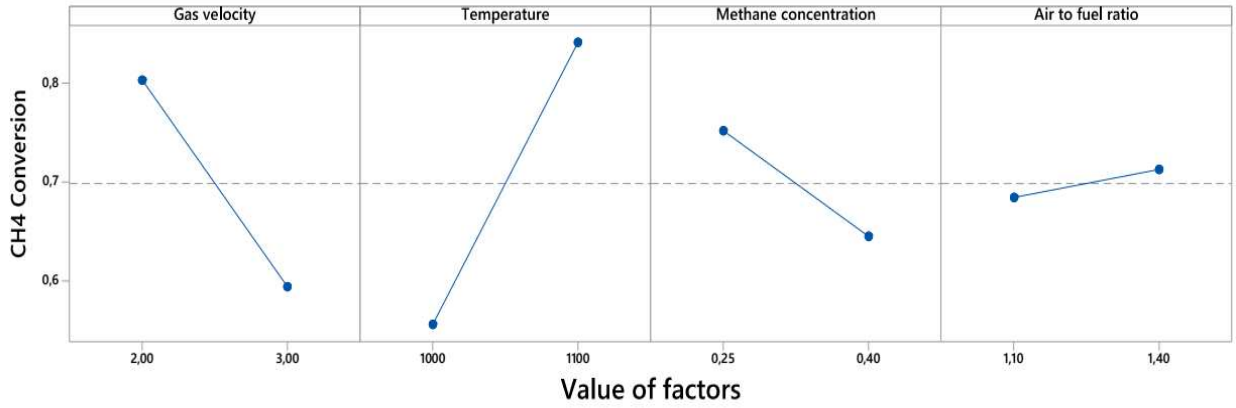

Figure 10: Main effect plot for CH_4 conversion

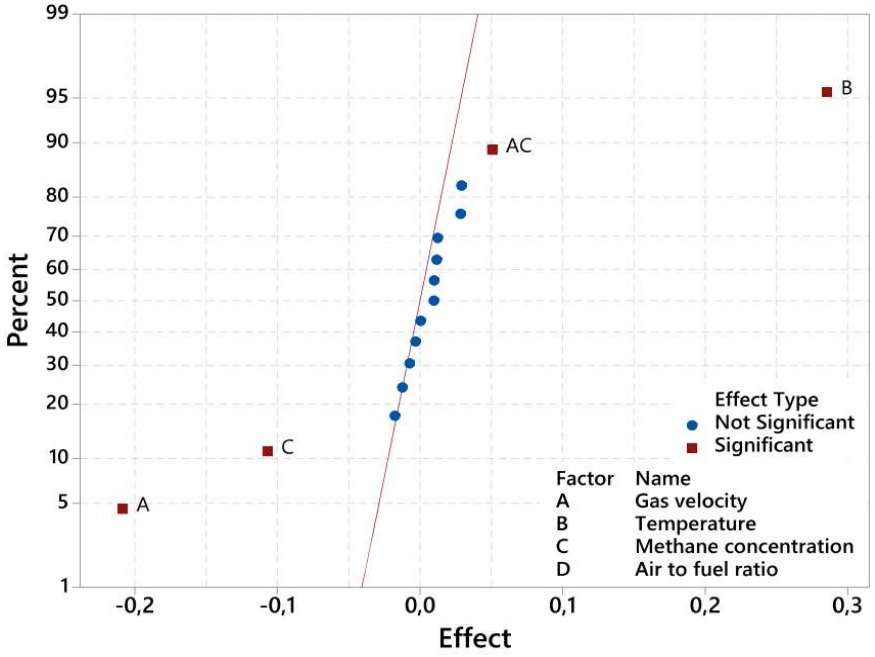

Figure 11: Normal plot of the effects

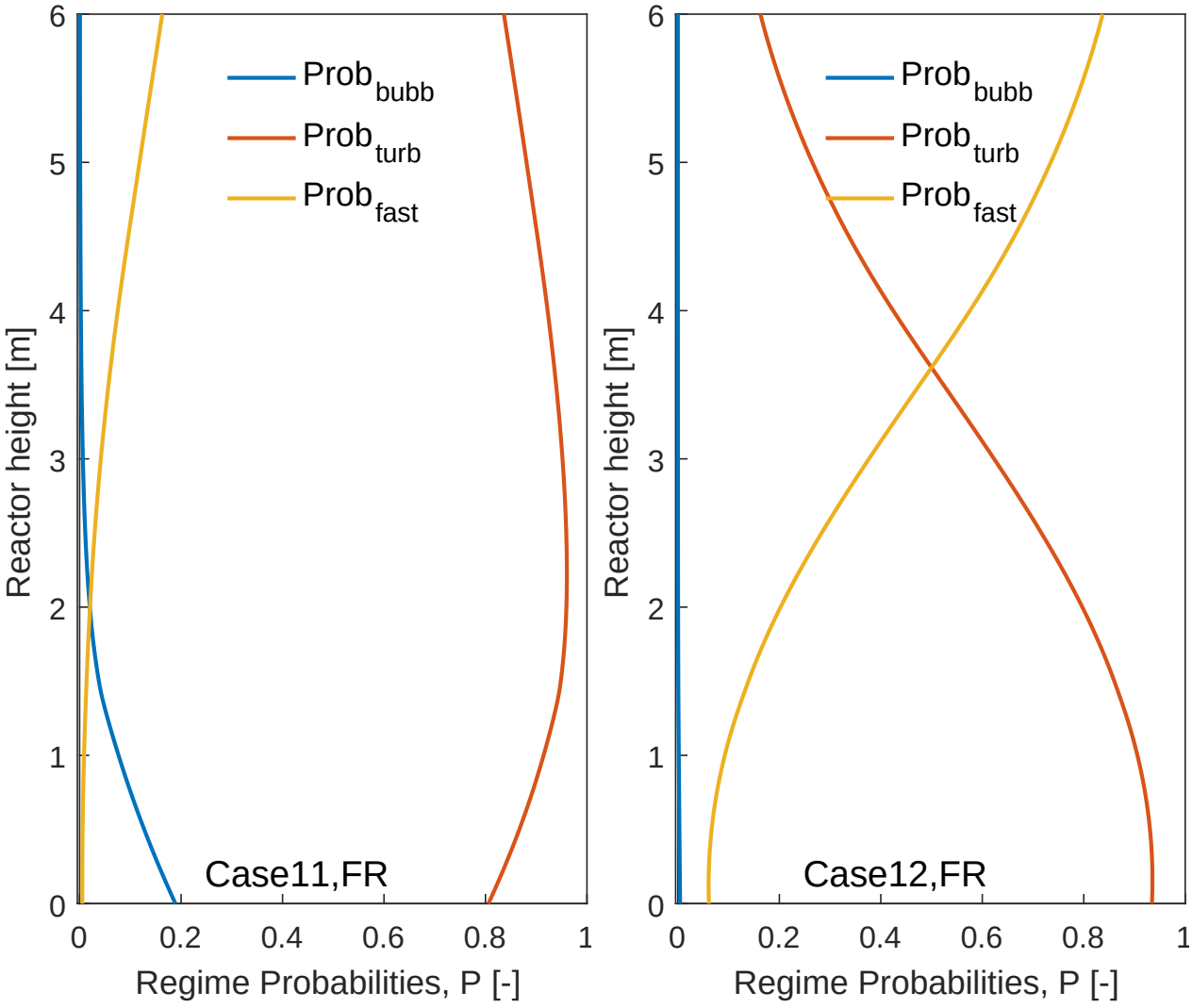

(a) (b)

Figure 12: Regime probability in FR (a) Case 11. (b) Case 12.

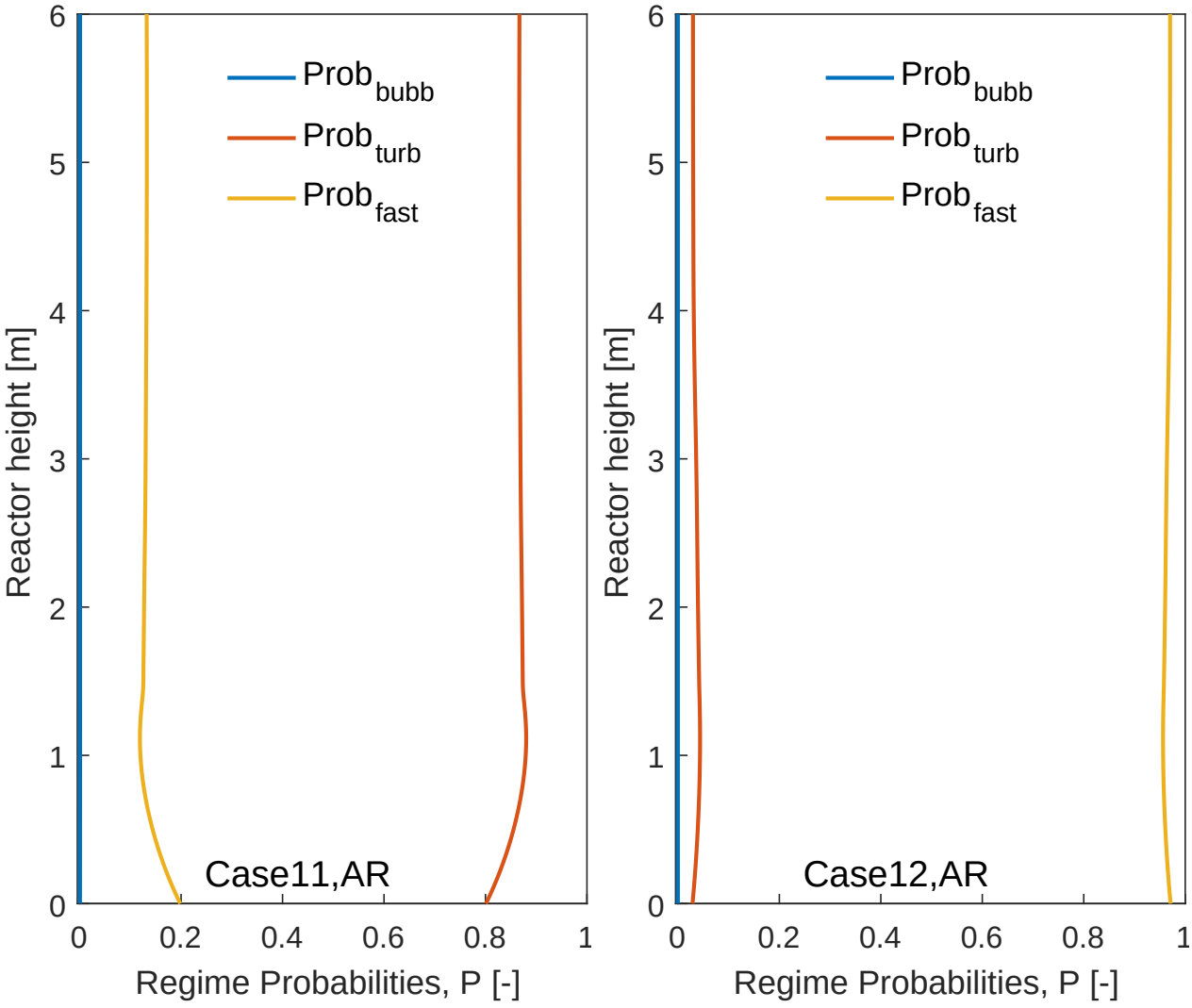

(a) (b)

Figure 13: Regime probability in AR (a) Case 11. (b) Case 12.

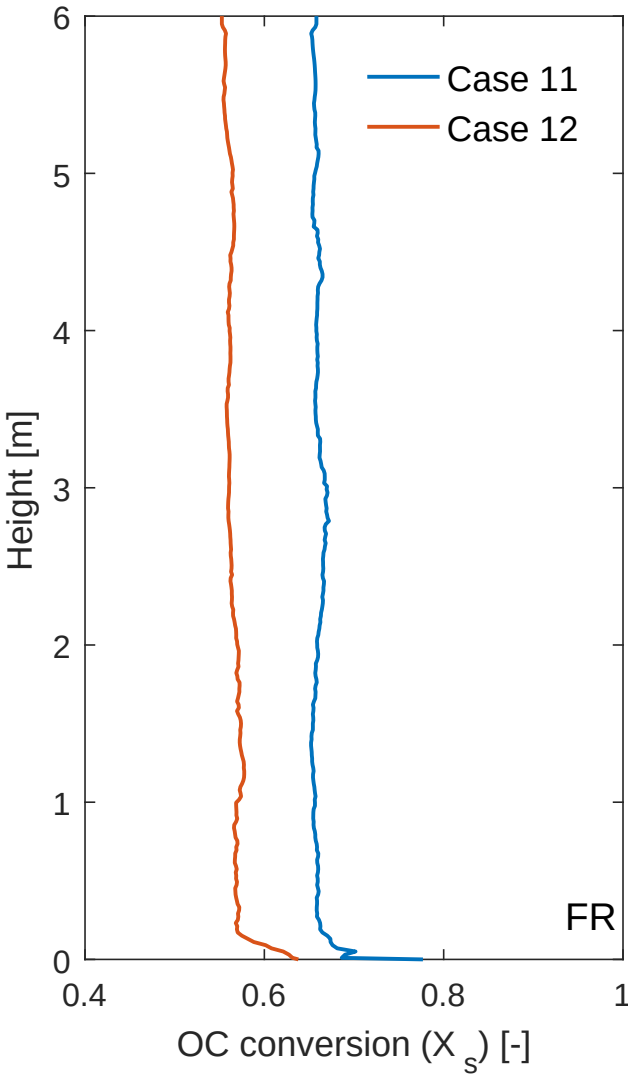

Figure 14: OC conversion

For Table of Contents Only